Direct Writing of Gallium-Indium Alloy for Stretchable Electronics

*J. William Boley, Edward L. White, George T.-C. Chiu, and Rebecca K. Kramer**

In this paper, a direct writing method for gallium-indium alloys is presented. The relationships between nozzle inner diameter, standoff distance, flow rate, and the resulting trace geometry are demonstrated. The interaction between the gallium oxide layer and the substrate is critically important in understanding the printing behavior of the liquid metal. The difference between receding and advancing contact angles demonstrates that the adhesion of the oxide layer to the substrate surface is stronger than the wetting of the surface by the gallium-indium alloy. This further demonstrates why free-standing structures such as the traces described herein can be realized. In addition to the basic characterization of the direct writing process, a design algorithm that is generalizable to a range of trace geometries is developed. This method is applied to the fabrication of an elastomer-encapsulated strain gauge that displays an approximately linear behavior through 50% strain with a gauge factor of 1.5.

1. Introduction

Recent progress in biocompatible and biomimetic devices has seen an influx of gallium-indium (Ga–In) alloys for stretchable conductors and sensors. Attractive attributes of these types of materials, such as low melting temperatures, low resistivity ($\approx 29 \times 10^{-6}$ Ω cm)[1] and low viscosity (≈2.4 mPa s),[2] allow them to conform and stretch to many different configurations while maintaining an electrical connection. Additionally, the presence of a naturally formed oxide skin on the exposed surface of Ga–In alloy in standard conditions induces a high surface tension (≈ 0.6 N m^{-1}),[1] facilitating the formation of stable free-standing structures.[3] Recent applications include reversibly deformable and mechanically tunable fluidic antennas,[4] hyperelastic pressure sensors,[5] embedded elastomer conductors,[2] 3D highly stretchable conductors,[6] a stretchable radio frequency (RF) radiation sensor,[7] wearable tactile interfaces,[8,9] and soft curvature sensors for joint angle proprioception.[10]

In contrast, some of the properties of Ga–In alloys that attract its use as a functional material are the very same properties that make it difficult for additive, high throughput, scalable fabrication processes. For example, in the context of inkjet printing, the combination of viscosity, surface tension, and density alone suggest Ga–In alloy to be a non-printable fluid without modifying either the material or the atmosphere (Supporting Information). Additionally, the fast-forming oxide layer can easily clog a nozzle orifice, further increasing the difficulty of inkjet printing Ga–In alloys.

Although inkjet printing of Ga–In alloys has yet to come, there have been recent advancements made in printing Ga–In alloy-based structures. Tabatabai et al. applied micro contact printing to Ga–In alloys and successfully patterned dot arrays, lines, pads and a functioning comb capacitor on elastomer substrates.[11] Ladd et. al. pumped Ga–In alloy through a capillary in order to 3D print vertical columns and arbitrarily stackable connected pendant drops of conductive liquid.[12] Other direct writing methods such as dip-pen nanolithography[13] and functional paste extrusion[14] have been successfully employed for other types of functional materials.

Here, we propose a novel direct writing approach which complements the previously explored printing methods. This method is achieved by flowing eutectic Ga–In (EGaIn) (Sigma-Aldrich, 75% Ga, 25% In) through a blunt syringe needle in close proximity to a moving substrate. As shown in **Figure 1**, the flow rate Q is controlled through a syringe pump while the stage maps out a prescribed geometry (for example, the serpentine pattern given in Figure 1b) at a controlled velocity v under a stationary syringe needle of inner diameter ID held at a controlled standoff distance h_0 above the substrate. We experimented with two particular silicon-based substrates: glass and Polydimethylsiloxane (PDMS, Slygard R 184, 10:1 weight ratio). This method exploits the strong adhesion between EGaIn and the two types of silicon-based substrates, evident from the near zero receding contact angle observed herein, which facilitates the pinning of the written trace to the surface. The formation of the gallium-oxide skin during the direct writing process allows the written pattern to maintain its printed shape, even through the elastomer encapsulation process. Moreover, trace geometry characterization measurements are used to provide a direct writing design strategy to inform the selection of ID, Q, v, and h_0 to obtain a desired trace geometry. This additive method of fabrication mitigates the need for micro-machining, masks, or

J. W. Boley, E. L. White, Prof. G. T.-C. Chiu,
Prof. R. K. Kramer
School of Mechanical Engineering
Purdue University
585 Purdue Mall, West, Lafayette, IN 47907, USA
E-mail: rebeccakramer@purdue.edu

DOI: 10.1002/adfm.201303220

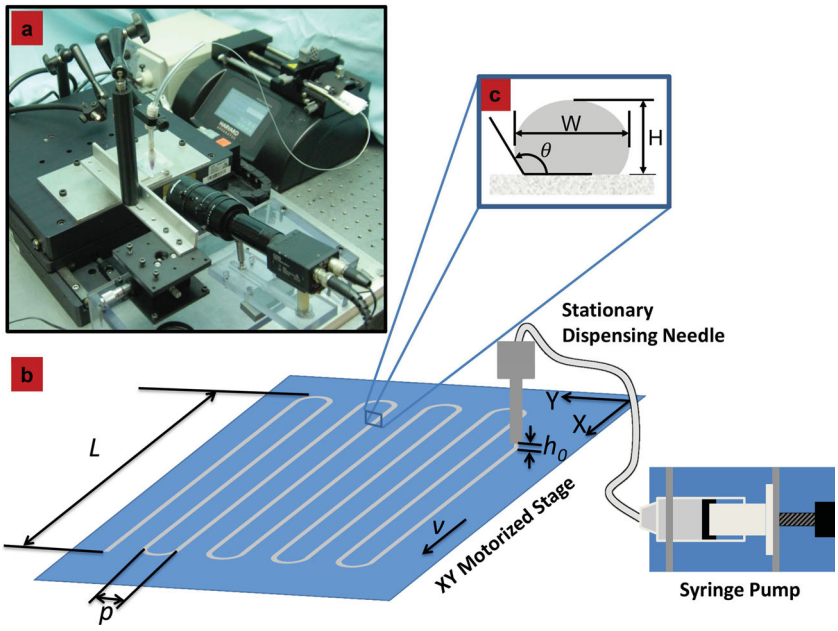

Figure 1. Direct writing system. a) Photograph of direct writing system. b) Schematic of direct writing system writing a serpentine pattern of length L, center-to-center line spacing p with a writing speed v, flow rate Q, and a needle standoff distance h_0. c) Detail cross-sectional view of a written trace of width W, height H, and contact angle θ.

molding processes while limiting the amount of waste material. Furthermore, this one-step fabrication method can be used in automated, high-volume applications while alleviating geometry limitations and pressure requirements previously encountered with filling microchannels. This work can be used in conjunction with other types of fabrication processes developed for Ga–In alloy as well, including masked deposition[2] and vacuum induced patterning.[6,15]

2. Results

2.1. Contact Angle Characterization

Figure 2a shows a summary of the contact angle measurements of EGaIn on glass and PDMS. In order to differentiate between the different contact angles within this study we introduce subscripts so that θ_a is the advancing contact angle, θ_s is the static contact angle, and θ_r is the receding contact angle. For the remainder of this paper, the contact angle of the written trace will simply be referred to as θ. The similarity in θ_a between glass (153.4° ± 3°) and PDMS (157.6° ± 3°) indicates similar spreading dynamics when EGaIn initially comes into contact with each of the surfaces. On the other hand, the large difference in θ_s between glass (128.6° ± 1.3°) and PDMS (150.0° ± 2°) indicates that EGaIn exhibits a higher level of wetting with glass compared to PDMS. In general, the results suggest low wettability between EGaIn and both substrates, since $\theta_s > 90°$. The resulting θ_r was found to be <10° for both glass and PDMS. In fact, a post-hoc visual inspection of the substrate revealed a thin layer of EGaIn remaining on the substrate, suggesting θ_r to be approaching 0°. Comparing these results to a previous study including measurements of θ_a and θ_r indicates similar surface interactions between Galinstan and PDMS ($\theta_a \approx 155°$ and $\theta_r \approx 6°$ for Galinstan on PDMS).[16]

Assuming that EGaIn behaves as a liquid, the energy E_r associated with removing EGaIn from each of the surfaces can be expressed using the equation for the work of adhesion.[17]

$$E_r = \gamma(1+\cos\theta_r) \quad (1)$$

where $\gamma \approx 0.6$ N m^{-1} is the surface tension of EGaIn. This yields $E_r \approx 2\gamma \approx 1.2$ N m^{-1}, indicating that the cohesion (≈0.5 N m^{-1})[3] of EGaIn is smaller than its adhesion to either of the substrates. This finding further explains why pump-filled microchannels of EGaIn maintained their shape without exiting the channel upon release of the pressure, as observed in previous studies;[3,10] reflow was prevented by the adhesion of the EGaIn to the PMDS microchannel walls. Another finding by Dickey et al.[3] is that EGaIn without the oxide layer will indeed reflow when the pump pressure is released. Corroborating this result with ours indicates that the oxide layer formed on the surface of the EGaIn maintains a strong adhesion to the two substrates, facilitating the direct writing of traces presented herein.

2.2. Characterization of Written Traces

Figure 2b shows optical micrographs of EGaIn traces realized by the direct writing system shown in Figure 1a with different nozzle inner diameters on glass and PDMS. In order to assess the quality of the written traces, line raggedness defined as the standard deviation of the residuals from a line fitted to the edge of the written trace,[18] was employed for each written trace in this study. The resulting line raggedness for each trace was normalized by its corresponding trace width for cross-comparison. This resulted in an average normalized line raggedness of 3% with a minimum value of 1% and a maximum value of 7%. Additionally, EGaIn trace height H and width W measurements were obtained in order to characterize effects of the system inputs (flow rate Q, needle inner diameter ID, standoff distance h_0, writing speed v, and substrate type) on the written trace geometry. The results from these measurements are summarized in Figures 2c–f.

Figure 2c shows representative trace widths for lines written onto glass and PDMS using needles with different inner diameter values. The relatively small 95% confidence intervals for the slopes (0.72 ± 0.06 for glass and 0.66 ± 0.06 for PDMS) and intercepts (–1.0 μm ± 10 μm for glass and –29 μm ± 9 μm for PDMS) indicate a linear scaling of the trace width with respect to ID. Although the slopes are similar, it is clear that the trace width for PDMS is consistently smaller than that of

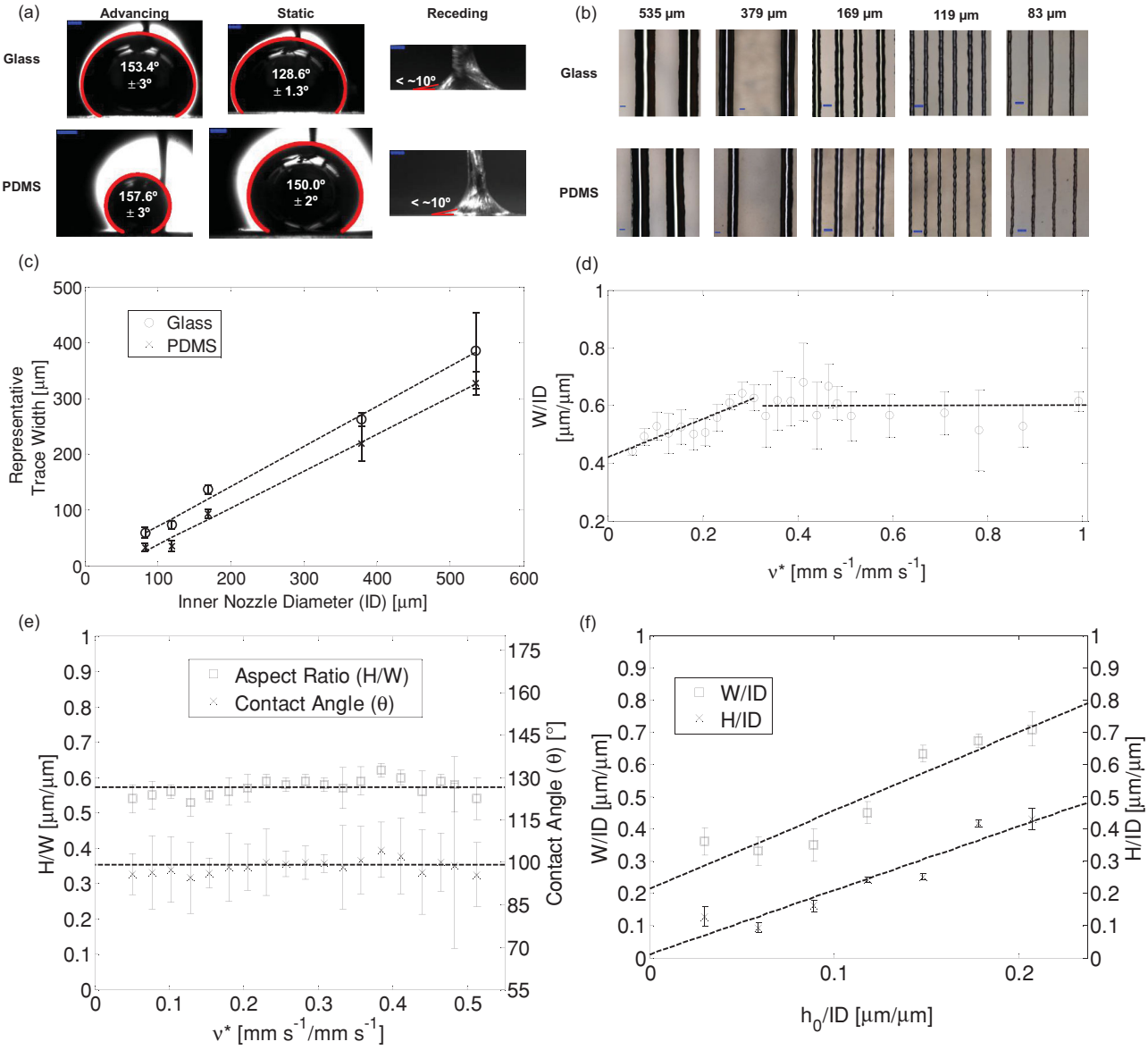

Figure 2. Characterization of directly written traces. a) Representative optical images extracted from contact angle videos (Supporting Information, Videos M1–M6) of sessile drops used to characterize the advancing, static and receding contact angle of EGaIn on glass and PDMS. Contact angle values imposed onto advancing and static images represent average measured contact angles and corresponding 95% confidence intervals. Lighter colored (red) outline of advancing and static sessile drop images are fitted profiles using the corresponding average contact angle (Equations (3),(al),[21] Srinivasan et al.).[21] Lighter colored (red) angle outline on receding images is present to illustrate the resulting approximated receding contact angle. Scale bars are 500 µm in length. b) Optical microscope images of directly written traces resulting from nozzles of varied inner diameters (*ID*) writing on glass and PDMS. Scale bars are 100 µm in length. c) Representative trace widths as a function of *ID* on glass and PDMS substrates. Dotted line represents linear least squares fit to the data. Errorbars represent 95% confidence intervals. d) Trace widths normalized by *ID* as a function of ν^* for $h_0/ID \approx 0.18$ on glass. First dotted line represents linear least squares fit to the first 11 data points. Second dotted line represents the mean value of the last 14 data points (≈0.6). Error bars represent 95% confidence intervals. e) Aspect ratio and corresponding trace contact angle as functions of normalized exit velocity on glass. Dotted lines represent the average aspect ratio and corresponding contact angle over all of the data. Errorbars represent 95% confidence intervals. f) Normalized trace width and height as functions of h_0/ID for $\nu^* \approx 0.99$ on glass. Dotted lines represent linear least squares fits to the data. Errorbars represent 95% confidence intervals.

glass, displaying the effect of θ_s on the trace width. In general, for a given trace cross-sectional area, higher wetting (lower θ_s) results in larger trace widths compared to lower wetting (higher θ_s), which is consistent with the measurements shown in Figure 2c.

Before further discussions on the written trace geometry, it is instructive to introduce the different parameters plotted in Figure 2d–f. The normalized trace width W/ID is the ratio of the measured trace width to the measured needle inner diameter (see Supporting Information, Figure S1 for details on

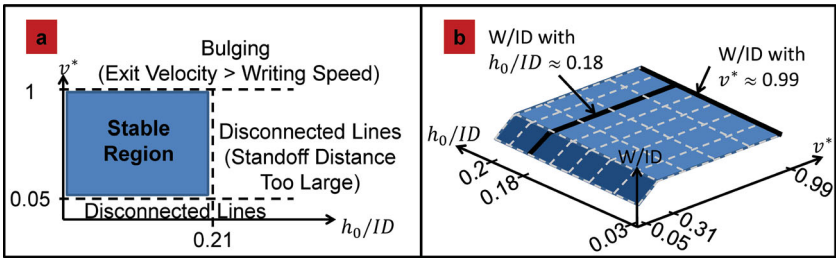

Figure 3. a) Stability region for written traces. Horizontal dotted lines represent upper and lower stable bounds for v^*. Vertical dotted line represents upper bound for h_0/ID, above which the lines become disconnected upon motion of the stage. b) Three dimensional surface used for design guidelines (constructed from Figures 2d–f). Bold black curves correspond to the data in Figures 2d,f.

measuring ID). Similarly, the normalized trace height H/ID is the ratio of the measured trace height to the measured needle inner diameter. Assuming no change in fluid density throughout the tubing and needle and equivalence between the cross-section of the needle and that of the EGaIn at the needle exit, the ratio of the velocity of the EGaIn exiting the needle to the stage velocity v^* is defined as

$$v^* = \frac{4Q}{\pi ID^2 v} \tag{2}$$

The aspect ratio (H/W) is simply the ratio of the trace height to the trace width. Finally, the normalized standoff distance h_0/ID is the ratio of the standoff distance to the needle inner diameter.

Figure 2d shows normalized trace width as a function of normalized exit velocity for EGaIn traces written on glass with $h_0/ID \approx 0.18$. The relatively small 95% confidence intervals on the slope (0.7 ± 0.2) and intercept (0.42 ± 0.05) of the fit indicates a linear effect of v^* on W/ID over the range of $0.05 \leq v^* \leq 0.31$. Interestingly, the increasing trend appears to saturate around $v^* \approx 0.31$, corresponding to $W/ID \approx 0.6$. This indicates an upper bound on W/ID with respect to v^*. As the height of the needle from the substrate is fixed in this experiment, it is expected that the presence of the needle is the source for the observed saturation (i.e. the constriction from the needle causes the contact area between the trace and substrate to increase so that θ approaches 90°, as illustrated in Supporting Information, Figure S2).

The effect of v^* on H/W and θ are summarized in Figure 2e. These values are relatively constant (95% confidence intervals of $H/W = 0.57 \pm 0.05$ and $\theta = 99° \pm 5°$). An interesting result shown in Figure 2e is $\theta < \theta_s$; in fact, $\theta \approx 0.77\theta_s$. This indicates that the internal pressure of the exiting EGaIn in this range of v^* is not large enough to cause the EGaIn to expand to the profile of a static sessile drop.

The above result is corroborated by the observed effect of h_0 on the profile of the printed EGaIn trace. Figure 2f shows the resulting normalized width and height measurements of traces written on glass with $ID = 169$ μm and $v^* = 0.99$. As expected, height increases linearly with respect to h_0. Unexpectedly, we also observe an increase in width with increasing h_0. We hypothesize this trend to be caused by the proximity of the needle to the substrate and its effect on trace contact angle. For a fixed v^* and Q, cross-sectional area of the printed trace must be conserved, which implies a change in trace profile that is dependent on h_0. We believe that at low values of h_0 (when the needle is close to the substrate), the presence of the needle may distort the shape of the depositing EGaIn. Given the strong adhesion between EGaIn and a glass substrate (shown in Figure 2a), and previous studies showing that the oxide layer on the exposed EGaIn surface can resist surface stresses up to ≈0.5 N m^{-1} (Dickey et al.),[3] we infer that traces deposited at low h_0 are "pinned" with $\theta \leq 90°$. However, increasing h_0 reduces the amount of distortion from the needle, allowing the depositing trace to minimize its surface energy and approach the profile of a static sessile drop (with θ approaching θ_s).

Although there is a clear trend in Figure 2f, the measurement uncertainty associated with h_0 (≈ ±3 μm) results in large 95% confidence intervals for the slopes (2.43 ± 1.02 for W/ID and 1.99 ± 0.77 for H/ID) and intercepts (0.08 ± 0.14 for W/ID and 0.01 ± 0.10 for H/ID) of the fitted linear models. Decreasing the uncertainty associated with h_0 would need to be realized in order to address this caveat. However, $h_0 << ID$ in our experiments, which indicates that the cross-sectional area of the printed trace is primarily governed by ID.

2.3. Stability of Written Traces

Stability limits for h_0/ID and v^* were observed during this study and are summarized in **Figure 3**a. To begin, for $h_0/ID > \approx 0.21$, the needle is too high off the substrate for stable traces to be achieved, indicating this value for h_0/ID as an upper bound. Although no lower limit on h_0/ID was observed, it is expected that stability is an issue as h_0/ID approaches 0, at which point pressure spikes could occur in addition to the mechanical limit.

In addition, traces written with $v^* < 0.05$ exhibited breaks/discontinuities, suggesting a lower limit on the normalized trace width. This occurs because the flow rate is not high enough to maintain stable EGaIn deposition, causing the exiting EGaIn to stretch and fracture. On the other hand, traces written with $v^* > 1$ are likely to exhibit abrupt bulges during the writing process as a result of the exit velocity being larger than the writing speed.

2.4. General Guidelines for Written Trace Design

As summarized in Figure 3a, the results from this study indicate a region within the space of input parameters v^* and h_0/ID that should be maintained for stable directly written traces. Any combination lying well within this region ($0 < h_0/ID < 0.21$ and $0.05 < v^* < 1$) should result in process stability.

The results summarized in Figures 2d–f are presented in dimensionless form so that they may be used as a guide for input parameter selection to achieve a desired trace geometry. Adopting a first order approximation and using the data

from Figures 2d–f, two intersecting planes can be formed (as shown in Figure 3b) to map out all achievable values for trace geometry.

2.4.1. $0.05 \leq \nu^* \leq 0.31$

Knowing the desired width and height of the trace to be printed, an appropriate ID can be selected given that W/ID can take on values between ≈ 0.1 (corresponding to $\nu^* \approx 0.05$ and $h_0/ID \approx 0.03$ in Figure 3b) and ≈ 0.7 ($\nu^* \approx 0.99$ and $h_0/ID \approx 0.2$). In addition, Figure 3b denotes that H/ID can take on values between ≈ 0.06 ($\nu^* \approx 0.05$ and $h_0/ID \approx 0.03$) and ≈ 0.42 ($\nu^* \approx 0.99$ and $h_0/ID \approx 0.2$). Once ID is chosen, h_0/ID and ν^* can be found using

$$\begin{bmatrix} \frac{h_0}{ID} \\ \nu^* \end{bmatrix} = \frac{1}{ID}\begin{bmatrix} -73.89 & 133.33 \\ 18.89 & -33.33 \end{bmatrix}\begin{bmatrix} H \\ W \end{bmatrix} \quad (3)$$

which represents the plane corresponding to the range of ν^* included in the set [0.05, 0.31] in Figure 3b. If ν^* is indeed found to be within this range, then the design is complete and the ratio Q/ν may be found via substitution with Equation (2).

2.4.2. $0.32 \leq \nu^* \leq 1$

If $\nu^* > 0.31$, the solution must fall within the plane corresponding to the range of $0.32 \leq \nu^* \leq 1$, hence a ν^* value within this plane must be selected. As trace width and height are coupled (linearly dependent) in this regime, only one critical dimension can be selected in conjunction with ν^*, while the corresponding h_0 and H or W can be derived from Figure 2f. Assuming the width to be the critical dimension, h_0/ID is given as:

$$\frac{h_0}{ID} = \frac{W/ID - 0.17}{2.4} \quad (4)$$

and the resulting height can be computed by:

$$H = 2.1h_0 - 0.03ID \quad (5)$$

Alternatively, if height is the preferred critical dimension, h_0/ID can be found using:

$$\frac{h_0}{ID} = \frac{H/ID + 0.03}{2.1} \quad (6)$$

and W is calculated with Equation (4).

Finally, ν and Q can be tuned to satisfy Equation (2), which gives some design freedom to adapt the process to throughput requirements.

2.5. Stretchable Strain Gauge Via Direct Writing

Figure 4 highlights an application of this direct writing method to strain gauge devices. The main image in Figure 4a demonstrates repeatability of the process. To demonstrate device scalability, the inset is included in Figure 4a showing a larger scale device with accompanying contact pads. The featured contact pads were also written by the direct writing process with the line spacing p set sufficiently small so that consecutive traces coalesce. Strain gauges written directly onto PDMS were then encapsulated in PDMS for performance characterization, summarized in Figure 4b. The resistance increase is roughly linear with strains up to 50%, with an approximate slope (gauge factor) of 1.5. However, resistance dependency deviates from the linear trend with strains greater than 50%, which is in agreement with previous studies.[19,20]

3. Discussion

The direct writing method and results reported in this work demonstrate a rapid, repeatable, scalable, maskless, one-step additive method for fabricating uniform continuous films. Another key feature of this method is its ability to directly write a liquid such as EGaIn that exhibits properties indicative of a non-printable fluid with respect to inkjet technology, indicating extension of this method to the direct writing of other liquids that are problematic for other patterning methods, provided $\theta_r << \theta_s$ for the liquid/substrate interface. Other functional liquids of potential interest include suspensions with high concentrations of nano-particles, polymers, and ionic liquids. Furthermore, the scalability observed within this method suggests possible extension to scales ranging from nanometer to millimeter, provided appropriate needle sizes are used (see Supporting Information Figure S1 for ID measurements pertaining to this study).

The restricted amount of control on h_0 limits the current system to a single layer. However, this limitation is currently being addressed by incorporating a motorized z-stage and feedback controller, which will facilitate 3D writing via stacking of additional layers structurally enabled by the inter-layer oxide skin, as previously demonstrated with spheres of EGaIn.[12] The results presented are provided to serve as a guide for tuning the input parameters in order to print a single-layer trace. However, the actual outcome may vary depending on the substrate, writing material, and system specifications. Furthermore, future work can be done in order to verify the constant flow rate of the extruder. We expect that further optimization of the process will facilitate the ability to rapidly create novel devices and electronics, such as conformable inductors and capacitors, with applications in conformable sensing/actuating skins, robotics, medical devices, conformable orthotics, and stretchable electronics.

4. Experimental Section

Preparation of PDMS: The Slygard 184 two-part PDMS was received from Dow Corning. The monomer and hardener were mixed together at a 10:1 weight ratio in a THINKY ARE-310 planetary centrifugal mixer. The mixture was spun in the mixer at 2000 rpm for 30 s (mixing), immediately followed by 2200 rpm for 30 s (degassing).

Preparation of Substrates Used: The glass substrates employed for direct writing were Gold Seal pre-cleaned 75 mm × 25 mm × 1 mm glass slides and were used as received. The PDMS substrates were made by

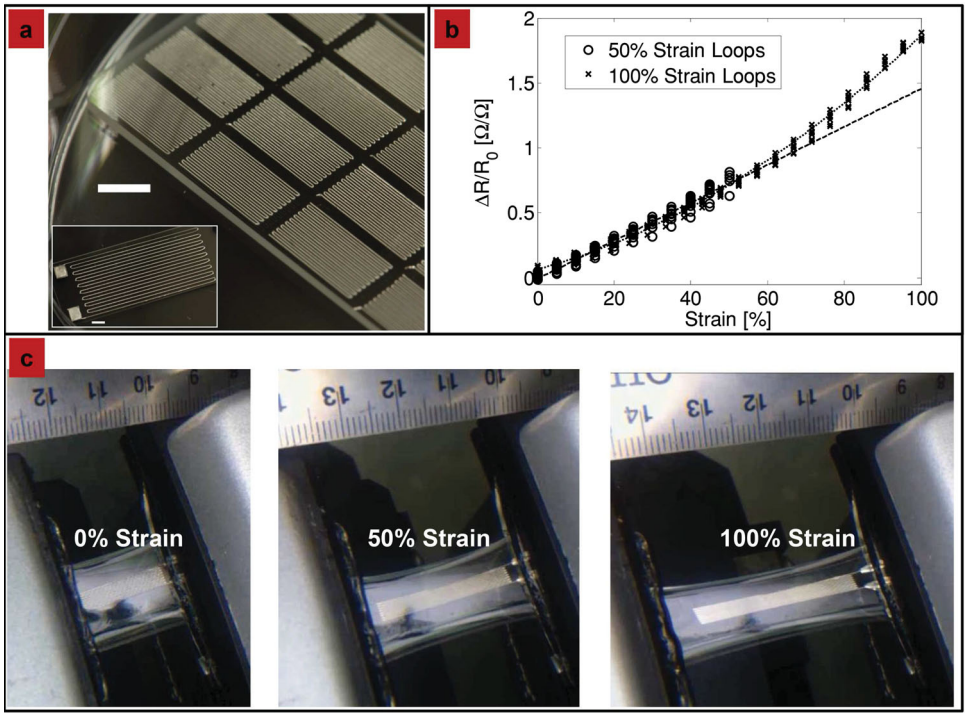

Figure 4. Application of direct writing to strain gauge devices. a) (main image) Photograph of multiple strain gauge devices on glass. Scale bar is 5 mm in length. Patterns were written using the 119 μm inner diameter nozzle. (inset) Photograph of a larger scale directly written strain gauge on glass. Scale bar is 5 mm in length. Device and pads were written using a 379 μm inner diameter nozzle. b) Performance characterization of directly written strain gauges encapsulated in PDMS. Both loops (50% strain and 100% strain) were repeated for five cycles. Dashed line is a linear least squares fit through the 50% strain data. Double dashed line is a quadratic least squares fit through the 100% strain data. $R_0 = 50\ \Omega$ for the 50% trials, with a corresponding unstretched length of 20 mm. $R_0 = 64\ \Omega$ for the 100% strain trials, with a corresponding unstretched length of 21 mm. c) Photographs of characterized strain gauge stretched at different strains throughout experiment. Smallest deviations on ruler represent one millimeter.

spin coating the PDMS mixture onto Corning 75 mm × 50 mm × 1 mm glass slides. The glass slides were pre-treated with Mann Ease Release 200 to better facilitate removal of devices post encapsulation. The PDMS mixture was then spin coated onto the pre-treated glass slides at 400 rpm for 50 s with 10 s ramp up and ramp down times. This resulted in a PDMS layer of approximately 50 μm according to theory (Equation 3.18 of Krishnan).[21] The PDMS coated glass slides were then placed in an incubator (Shell Lab GI2) at 60 °C for two hours to cure.

Experimental Details of Direct Writing System: The system used for the direct writing experiments is featured in Figure 1. Lines of EGaIn were directly written using a stationary blunt syringe needle (details of syringe tips can be found in Supporting Information Figure S1) and pump (Harvard Apparatus PHD Ultra 4400) system coupled with a motorized XY stage (Anorad WKY-150) and an optical imaging camera. Details of the motorized XY stage are reported elsewhere.[22] For each experiment, EGaIn was supplied to the syringe needle at a constant flow rate Q by means of the syringe pump and tubing as shown in Figure 1. The height h_0 between the syringe needle and the substrate was held constant (≈ ±3 μm) for each experiment and controlled using a manual z-stage (Edmund Optics 56–335) for height adjustment and CCD camera for visually detecting when the needle comes in contact with the substrate (i.e., $h_0 = 0$). To initiate direct writing the stage was moved to the starting point of the pattern. Upon reaching the starting position, h_0 was set to zero in order to make contact between the liquid meniscus and the substrate. Next, h_0 was set to its desired value. Finally, the stage motion was activated by means of a pre-programmed motion profile dynamically controlled via a motion controller (Anorad CM-2). The preset flow rate Q from the pump began immediately after the start of the stage motion. The pump was stopped upon the end of the stage motion. Detachment of the EGaIn within the needle from the written pattern was realized by simultaneously increasing h_0 and moving the pattern from the needle via XY stage at a high velocity in order to overcome the surface tension of the EGaIn (see Supporting Information Video M7 for a direct writing example of a serpentine pattern).

Encapsulating and Wiring Devices: The written devices were encased by spin coating PDMS over the devices at 400 rpm for 50 s with 10 s ramp up and ramp down times. Post-hoc inspection showed that the added mechanical strength of the Ga oxide layer facilitated the structural integrity of the device during the spin encasing process, as seen with other studies.[3,11,12] The encased devices were then placed in an incubator at 60°C for two hours to cure. After curing, the bottom edges of the device contact pads were removed from each device by means of an X-acto knife. Copper wires were then inserted into the remaining portion of the contact pads and the incisions were covered with a few additional drops of PDMS. Finally, the devices were placed in an incubator again at 60 °C for two hours in order for the additional drops of PDMS to cure.

Characterization: The trace height and widths were measured using a laser confocal microscope (LEXT 3000) with a 50X microscope objective. Contact angle measurements were obtained using the sessile drop method. Advancing sessile drops were produced by pushing EGaIn out of a needle in close proximity to the substrate at a controlled flow rate (≈100 μL min^{-1}). Static sessile drops were made by stopping the flow rate of the advancing sessile drops and allowing for relaxation of the drop to equilibrium. The advancing and static contact angles were obtained by applying the perturbation solution of the Bashforth-Adams equation presented by Srinivasan et al.[23] The sessile drop height and width data used in the perturbation solution was obtained by analyzing the advancing and static contact angle videos (Supporting Information, Videos M1,M2,M4,M5) via MATLAB's image processing toolbox. The receding contact angles were estimated visually from the video (Supporting Information, Videos M4,M6) images, since the embedded

needle made it difficult to extract height data for the receding cases. It should be noted that post-hoc visual inspection of the substrates revealed EGaIn films remained on the surface, indicating a near-zero θ_r for both substrates. For the strain gauge characterization, one side of the strain gauge was mounted in a vice fixed to the XY stage while the other side was mounted to a vice fixed to the stationary optical table as shown in Figure 4. Upon measuring the unstretched length with a ruler, the strain gauge underwent stretching cycles with 1 mm steps of the XY stage. The corresponding resistance was measured using a digital multimeter (Fluke 87V) directly after each step.

Supporting Information

Supporting Information is available from the Wiley Online Library or from the author.

Acknowledgements

The authors would like to Dr. Peroulis and his research group, specifically Colby Barlett, Juan Zeng, Nithin Raghunathan, and Anurag Garg, for access to and training on equipment used for this study.

Received: September 17, 2013
Revised: December 30, 2013
Published online: February 18, 2014

[1] D. Zrnic, D. S. Swatik, *J. Less Common Met.* **1969**, *18*, 1.
[2] R. K. Kramer, C. Majidi, R. J. Wood, *Adv. Funct. Mater.* **2013**, *23*, 42.
[3] M. D. Dickey, R. C. Chiechi, R. J. Larsen, E. A. Weiss, D. A. Weitz, G. M. Whitesides, *Adv. Funct. Mater.* **2008**, *18*, 7.
[4] J. H. So, J. Thelen, A. Qusba, G. J. Hayes, G. Lazzi, M. D. Dickey, *Adv. Funct. Mater.* **2009**, *19*, 22.
[5] Y. L. Park, C. Majidi, R. Kramer, P. Bérard, R. J. Wood, *J. Micromech. Microeng.* **2010**, *20*, 12.
[6] J. Park, S. Wang, M. Li, C. Ahn, J. K. Hyun, D. S. Kim, J. A. Rogers, Y. Huang, S. Jeon, *Nat. Commun.* **2012**, *3*, 916.
[7] S. Cheng, Z. Wu, *Lab Chip* **2010**, *10*, 23.
[8] R. K. Kramer, C. Majidi, R. J. Wood, *IEEE Int. Conf. Robotics Automation (ICRA)* **2011**.
[9] R. D. Ponce Wong, J. D. Posner, V. J. Santos, *Sens. Actuators A: Phys.* **2012**, 179.
[10] R. K. Kramer, C. Majidi, R. Sahai, R. J. Wood, *IEEE RSJ Int. Conf. Intelligent Robots Syst. (IROS)* **2011**.
[11] A. Tabatabai, A. Fassler, C. Usiak, C. Majidi, *Langmuir* **2013**, *29*, 20.
[12] C. Ladd, J. H. So, J. Muth, M. D. Dickey, *Adv. Mater.* **2013**, *25*, 36.
[13] R. D. Piner, J. Zhu, F. Xu, S. Hong, C. A. Mirkin, *Science* **1999**, *283*, 5402.
[14] B. Y. Ahn, E. B. Duoss, M. J. Motala, X. Guo, S.-I. Park, Y. Xiong, J. Yoon, R. G. Nuzzo, J. A. Rogers, J. A. Lewis, *Science* **2009**, *323*, 5921.
[15] B. L. Cumby, G. J. Hayes, M. D. Dickey, R. S. Justice, C. E. Tabor, J. C. Heikenfeld, *Appl. Phys. Lett.* **2012**, *101*, 17.
[16] G. Li, M. Parmar, D. Kim, J. B. J. Lee, D. W. Lee, *Lab Chip* **2014**, *14*, 1.
[17] N. K. Adam, H. K. Livingston, *Nature* **1958**, *182*, 128.
[18] ISO 13660 – Information technology – Office equipment – Measurement of image quality attributes for hardcopy output – Binary monochrome text and graphic images (**2001**).
[19] H. J. Kim, T. Maleki, P. Wei, B. Ziaie, *J. Microelectromech. Syst.* **2009**, *18*, 1.
[20] S. Zhu, J. H. So, R. Mays, S. Desai, W. R. Barnes, B. Pourdeyhimi, M. D. Dickey, *Adv. Funct. Mater.* **2012**, *23*, 18.
[21] S. Krishnan, Ph.D. Thesis, Massachusetts Institute of Technology, **2007.**
[22] A. K. Adak, J. W. Boley, D. P. Lyvers, G. T. Chiu, P. S. Low, R. Reifenberger, A. Wei, *ACS Appl. Mater. Interfaces* **2013**, *5*, 13.
[23] S. Srinivasan, G. H. McKinley, R. E. Cohen, *Langmuir* **2011**, *27*, 22.